Block-Copolymer-Assisted One-Pot Synthesis of Ordered Mesoporous WO_{3-x}/Carbon Nanocomposites as High-Rate-Performance Electrodes for Pseudocapacitors

Changshin Jo, Jongkook Hwang, Hannah Song, Anh Ha Dao, Yong-Tae Kim, Sang Hyup Lee, Seok Won Hong, Songhun Yoon, and Jinwoo Lee**

An ordered mesoporous tungsten-oxide/carbon (denoted as m-WO_{3-x}-C-s) nanocomposite is synthesized using a simple one-pot method using polystyrene-*block*-poly(ethylene oxide) (PS-*b*-PEO) as a structure-directing agent. The hydrophilic PEO block interacts with the carbon and tungsten precursors (resol polymer and WCl_6), and the PS block is converted to pores after heating at 700 °C under a nitrogen flow. The m-WO_{3-x}-C-s nanocomposite has a high Brunauer–Emmett–Teller (BET) surface area and hexagonally ordered pores. Because of its mesoporous structure and high intrinsic density of tungsten oxide, this material exhibits a high average volumetric capacitance and gravimetric capacitance as a pseudocapacitor electrode. In comparison with reduced mesoporous tungsten oxide (denoted as m-WO_{3-x}-h), which is synthesized by a tedious hard template approach and further reduction in a H_2/N_2 atmosphere, m-WO_{3-x}-C-s shows a high capacitance and enhanced rate performance, as confirmed by cyclic voltammetry, galvanostatic charge/discharge measurements, and electrochemical impedance spectroscopy. The good performance of m-WO_{3-x}-C-s is attributed to the high surface area arising from the mesoporous structure, the large interconnected mesopores, and the low internal resistance from the well-dispersed reduced tungsten oxide and amorphous carbon composite structure. Here, the amorphous carbon acts as an electrical pathway for effective pseudocapacitor behavior of WO_{3-x}.

1. Introduction

Electrochemical capacitors (ECs), also known as supercapacitors, with high power density and long cycle life have attracted much attention as promising energy-storage devices for use in smart grids, portable electronics, and electric vehicles (EVs).[1] Generally, pseudocapacitors accumulate charge by a faradaic reaction within the interface between the electrode and electrolyte, while electric double-layer capacitors (EDLCs) utilize the surface of the porous carbon for a non-faradaic reaction. Nowadays, because of the low energy densities of EDLCs, many researchers have focused on employing pseudocapacitor electrodes by using various transition metal oxides (RuO_2, NiO, and MnO_2)[2] and conducting polymers (polyaniline and polypyrrole).[3] In particular, some transition metal oxides such as RuO_2 and MnO_2 have been studied extensively because of their high specific capacitance arising from their fast and reversible redox reaction. However, in spite of their satisfactory pseudocapacitor performance, the high cost and toxic nature of RuO_2 and poor electrical conductivity of MnO_2 have been drawbacks for commercial applications. Therefore, in order to overcome these limitations, the pseudocapacitive materials have been loaded on conductive supports such as carbon nanotubes, porous carbon, porous metal, graphene, etc.[4] Although good cyclability and better performances have been achieved at slow charge/discharge rates, the achievement of high power density and energy density at high rates is still a challenge. In addition, only a small amount of active materials have been loaded on the current collector or conductive material for enhanced pseudocapacitor performance in some reports, which is not feasible for mass production and practical applications[5]; the approach for active material loading on conductive nanomaterials requires multiple steps.

Meanwhile, tungsten oxide (WO_3) is an attractive electrode material because of its low-cost and multiple oxidation states.[6] More importantly, the high intrinsic density (>7 g cm^{-3}) implies that WO_3 can be an alternative electrode material for small

C. Jo, J. Hwang, A. H. Dao, Prof. J. Lee
Department of Chemical Engineering
Pohang University of Science and Technology (POSTECH)
Pohang, Kyungbuk 790-784, Republic of Korea
E-mail: jinwoo03@postech.ac.kr
H. Song, Prof. Y.-T. Kim
Energy System Major, School of Mechanical Engineering
Pusan National University
Busan 609-735, Republic of Korea
Dr. S. H. Lee, Dr. S. W. Hong
Center for Water Resource Cycle Research
Korea Institute of Science and Technology
Hwarangno 14-gil 5, Seongbuk-gu, Seoul 136-791, Republic of Korea
Prof. S. Yoon
Department of Integrative Engineering
Chung-Ang University
221, Heukseok-Dong, Dongjak-Gu, Seoul, 156-756, Republic of Korea
E-mail: yoonshun@cau.ac.kr

DOI: 10.1002/adfm.201202682

size ECs system due to the high volumetric power/energy performance. To make high performance WO_3 electrodes, achievement of both increasing electrical conductivity of WO_3 (≈0.01 S cm^{-1} at 973 K)[7] for low total internal resistance and developing high surface nanostructured WO_3 through a facile synthetic method is highly required. However, until now there are a few reports on the pseudocapacitive performance of tungsten oxide materials.[6b–e]

Since the charge-storage reaction of both EDLCs and pseudocapacitors occurs on the electrode/electrolyte interface, considerable improvements to ECs have been achieved by introducing various nanostructured active materials. Among the variety of nanostructures used, ordered mesoporous structures have many advantages over other porous structures for supercapacitor applications.[8] The interconnected mesopores, with enlarged surface areas and short diffusion lengths, enhance the electron transport and the contact between the electrode and electrolyte. Furthermore, compared with nanoparticles, the micrometer-sized mesoporous particles exhibit more advantageous properties such as high electrode density and fast electron conduction between the particles.

We recently reported an efficient strategy for improving pseudocapacitive performance: the concept of reduced mesoporous metal oxides.[9] In our previous work, with a hard template approach (KIT-6 silica template), partially reduced mesoporous tungsten oxide (denoted as m-WO_{3-x}-h herein) was synthesized. As a pseudocapacitor electrode, the m-WO_{3-x}-h electrode exhibited a noticeable increase in rate capability and capacitance because of its higher electrical conductivity than m-WO_3 which have an identical porous structure (mesoporous tungsten trioxide, which has low electrical conductivity).[9b,9c] Moreover, the m-WO_{3-x}-h electrode showed a high volumetric capacitance as a result of its intrinsically high density.

Although the performance of tungsten oxide was improved by the mesoporous structure and partial reduction, it was revealed that the electrical conductivity decreased and proton resistance increased with voltage increase. It should be solved for the commercialization of tungsten-oxide electrode materials. In addition, the hard template approach requires multiple steps, consisting of the preparation of the silica template followed by impregnation of the precursor, heat treatment, partial reduction, and etching of the silica template.[10] From a practical point of view, a more convenient and straightforward synthetic strategy is required.

In this study, we report a facile 'one-pot' synthesis of ordered mesoporous reduced tungsten-oxide/carbon (denoted as m-WO_{3-x}-C-s) by the evaporation-induced self-assembly (EISA) method, which enhances the performance of tungsten oxide using a simple approach. The carbon precursor acts as a reducing agent during heat-treatment under an inert atmosphere, so the partially reduced tungsten-oxide particles are embedded in an amorphous conductive carbon framework. Another important aspect is that the nanosized carbon (heat-treated at 700 °C) constructs an electric double layer for charge storage, as well as improving the electrical conduction for the composite materials. Moreover, the structural merits of m-WO_{3-x}-C-s, such as its high surface area and ordered hexagonal mesopores, lead to its enhanced electrochemical performance. Interestingly, because of the high surface area and high intrinsic density of tungsten oxide, m-WO_{3-x}-C-s shows a high average volumetric capacitance (340 F cm^{-3}) and gravimetric capacitance (103 F g^{-1}). Moreover, the m-WO_{3-x}-C-s electrode exhibits a high rate performance because of the low internal resistance from the nanosized reduced tungsten oxide and the amorphous carbon composite structure. The interconnected structure of the composite material facilitates electron conduction,[11] and the proton of double layer on carbon surface could diffuse into the tungsten oxide at low voltage region.

2. Results and Discussion

2.1. Ordered Mesoporous Tungsten-Oxide/Carbon

The synthesis of the ordered mesoporous tungsten-oxide/carbon (m-WO_{3-x}-C-s) is summarized in **Scheme 1**. The laboratory-made amphiphilic block copolymer, poly(styrene-*b*-ethylene oxide) (PS-*b*-PEO), prepared by ATRP, was used as a structure-directing agent.[12] The hydrophilic inorganic precursors, resol polymer and WCl_6 hydrolyzed by anhydrous ethanol, interact with the hydrophilic PEO block via hydrogen bonding. During the EISA process, the mixture builds up into an ordered nanostructure. Finally, after calcination in a N_2 atmosphere at 700 °C, the m-WO_{3-x}-C-s nanocomposite is successfully synthesized.

The structure of the synthesized material was characterized by various analytical methods. The X-ray diffraction (XRD) results for m-WO_{3-x}-C-s are shown in **Figure 1**a. The diffraction

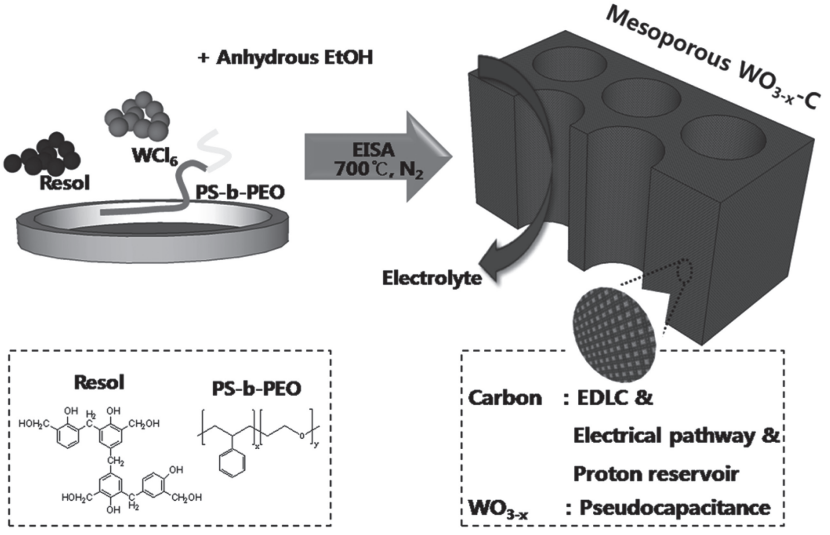

Scheme 1. Synthesis of mesoporous reduced tungsten-oxide/carbon nanocomposite (m-WO_{3-x}-C-s).

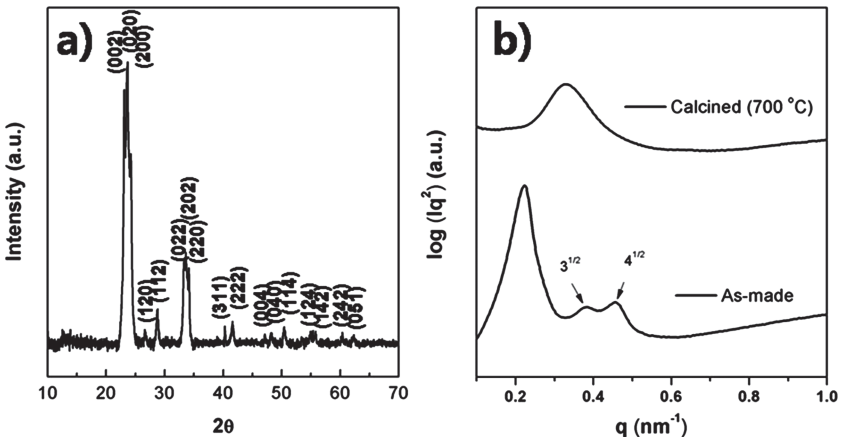

Figure 1. a) XRD pattern (JCPDS: 83-0948), b) SAXS traces before and after calcination.

peaks of m-WO_{3-x}-C-s are in good agreement with the patterns for anorthic WO_3 (JCPDS: 83-0948). We assume that the carbon precursor (the resol polymer) acts as a reducing agent and generates oxygen defects during the carbothermal reduction process.[13] The partial reduction of tungsten trioxide (8% of W^{5+}) in m-WO_{3-x}-C-s can be identified by X-ray photoelectron spectroscopy (XPS; Figure S1 in the Supporting Information). The intervalence charge transfer between W^{5+} and W^{6+} ions gives high electrical conductivity to tungsten oxide nanoparticles.[14] This partially reduced tungsten trioxide and amorphous carbon (calcined at 700 °C) nanocomposite is beneficial for high-rate pseudocapacitor application because of its enhanced electrical conduction compared to that of pure tungsten oxide.

Small-angle X-ray scattering (SAXS) patterns of the as-prepared sample and m-WO_{3-x}-C-s are shown in Figure 1b. The SAXS peaks of the as-prepared m-WO_{3-x}-C-s with the position ratios of $1:3^{1/2}:4^{1/2}$ indicate that this sample has long-range-ordered 2-D hexagonal pores. The main peak $d_{spacing}$ value (d_{100}) of the as-prepared sample is 27.6 nm. After calcination, the SAXS result for m-WO_{3-x}-C-s shows one single intense peak, which means that the hexagonal mesoporous structure is preserved but there is some loss of long-range order.[15] As seen on the graph, the peak is shifted to a larger q value (d_{100} value of m-WO_{3-x}-C-s: 19.6 nm) owing to shrinkage during the removal of organic molecules and the development of inorganic materials at high temperatures.

The pore structure of m-WO_{3-x}-C-s was characterized by nitrogen sorption analysis. **Figure 2**a shows the Barrett–Joyner–Halenda (BJH) pore-size distribution calculated from the adsorption branch of the nitrogen sorption isotherms (inset). The steep increase in adsorption at ≈0.8 P/P_0 indicates that uniform mesopores (12 nm) are well developed during the PS block decomposition. The Brunauer–Emmett–Teller (BET) surface area (A_{BET}) and single point total pore volume of m-WO_{3-x}-C-s are 123 $m^2\ g^{-1}$ and 0.07 $cm^3\ g^{-1}$, respectively. The small total pore volume of m-WO_{3-x}-C-s is caused by the high density of tungsten oxide. Since reduced WO_3 has the same crystalline structure as anorthic WO_3, we assumed that WO_{3-x} in the mesostructured walls has the same density as WO_3. The theoretical density (d_{cal}) of m-WO_{3-x}-C-s found by simple calculation using the pore volume and intrinsic density is 3.3 g cm^{-3} (see the calculation of density in the Supporting Information). Further studies on the mesopore structure of m-WO_{3-x}-C-s can be conducted by transmission electron microscopy (TEM). In Figure 2b, ordered hexagonal channel arrays with uniform and ordered cylindrical-type mesopores are clearly exposed in the images. The high-resolution TEM (HRTEM) (Figure S3 in the Supporting Information) shows a few nanometer sized tungsten oxide poly crystallites and amorphous carbon construct the ordered porous structure. Some of WO_{3-x} particles are embedded in the carbon matrix while the others are exposed to the surface. Figure S4 shows the Raman spectrum of m-WO_{3-x}-C-s, showing two bands around 1350 cm^{-1} and 1590 cm^{-1} from disordered carbon (D-band) and graphitic carbon (G-band), respectively.[16] The carbon content of the composite material is 24 wt% from thermogravimetric analysis (TGA) and CHN elemental analysis.

2.2. Electrochemical Characterization

In order to estimate the electrochemical performance of the synthesized materials, cyclic voltammetry (CV) was performed in the potential range –0.2 to 0.8 V in a cell with a three-electrode configuration (**Figure 3**). For the control experiment, m-WO_{3-x}-h synthesized with a hard template approach (KIT-6 template, Figure S5 in the Supporting Information) was also tested under the same conditions. This material is a partially reduced form of mesoporous tungsten oxide, prepared by heat treatment in a H_2/N_2 atmosphere.[9a] Figure 3a shows the CV curves of the m-WO_{3-x}-C-s and m-WO_{3-x}-h electrodes at 1 mV s^{-1}. The m-WO_{3-x}-h electrode shows a characteristic redox

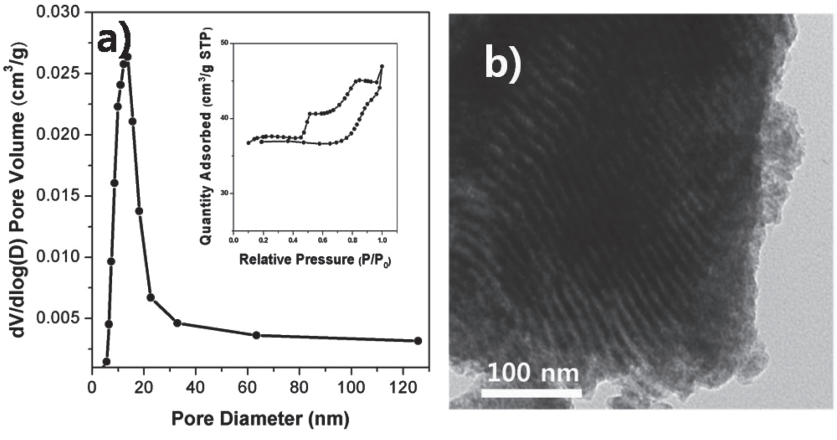

Figure 2. a) BJH pore-size distribution curve and N_2 adsorption-desorption isotherms (inset). b) TEM image of m-WO_{3-x}-C-s, viewed from the [110] direction.

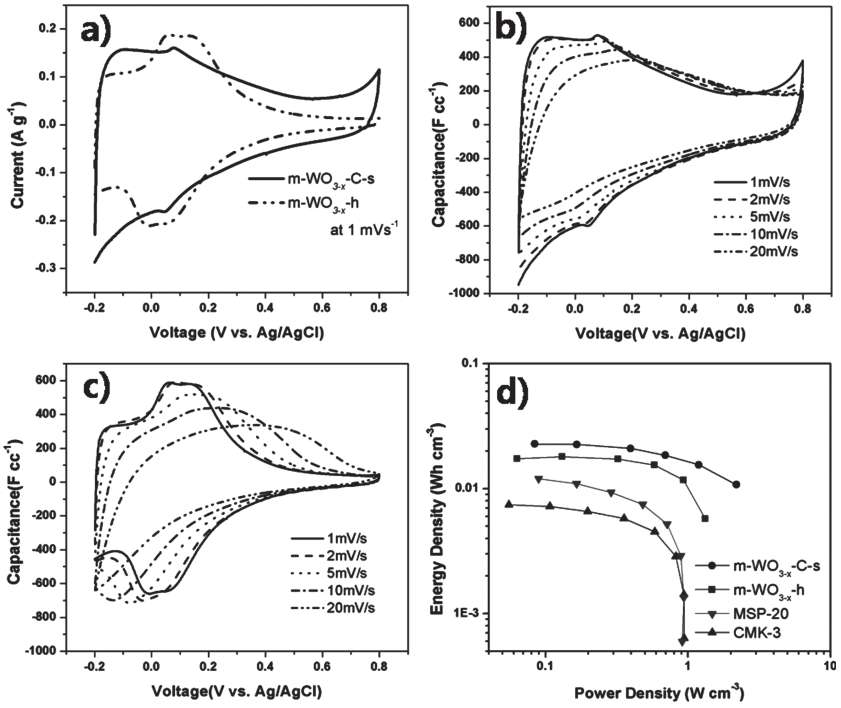

Figure 3. a) Cyclic voltammograms of m-WO_{3-x}-C-s and m-WO_{3-x}-h at a scan rate of 1 mV s^{-1}. Capacitance versus voltage profiles of b) m-WO_{3-x}-C-s and c) m-WO_{3-x}-h at a scan rate of 1–20 mV s^{-1}. d) Volumetric energy density versus power density plots of m-WO_{3-x}-C-s, m-WO_{3-x}-h, MSP-20, and CMK-3, calculated from CV measurements.

peak in the region near 0 V, which coincides with our previous study.[9b,c] In the m-WO_{3-x}-C-s electrode, however, a slightly decreased redox current was observed near 0.05 V but higher current was maintained in a wide voltage range. In addition, the CV curve area of the m-WO_{3-x}-C-s electrode is 31% higher than that of the m-WO_{3-x}-h electrode in spite of lower content of W^{5+} in m-WO_{3-x}-C-s (8%) than m-WO_{3-x}-h (15.8%) as shown in Figure S6. This reflects that the higher available charge can be accumulated in m-WO_{3-x}-C-s electrode than m-WO_{3-x}-h. From CV profiles, furthermore, the average specific capacitance (C_{cv}) can be calculated using following equation:[17]

$$C_{CV}(\nu) = \frac{1}{2m\Delta V}[Q_a(\nu) + Q_c(\nu)] \quad (1)$$

Here, ν is the scan rate, m is the weight of the active material, and Q_a and Q_c are the anodic and cathodic charges, respectively. From Figure 3a), the average specific capacitance (C_{sp_av}) of the m-WO_{3-x}-C-s electrode (103 F g^{-1}) is larger than that of the m-WO_{3-x}-h electrode (81 F g^{-1}), which is reasonable when considered with higher surface area of the former material as listed in **Table 1**. In addition, d_{cal} values were calculated for both materials (see Supporiting Information). Interestingly, d_{cal} of m-WO_{3-x}-C-s (3.3 g cm^{-3}) is even larger than that of m-WO_{3-x}-h (3.13 g cm^{-3}). Hence, much higher average volumetric capacitance (C_{vol_av}) of m-WO_{3-x}-C-s (340 F cm^{-3}) is obtained compared with C_{vol_av} of m-WO_{3-x}-h (254 F cm^{-3}); $C_{vol\_av} = C_{sp\_av} \times d_{cal}$, which is attributable to more optimized pore structure in m-WO_{3-x}-C-s for better charge utilization. In addition, average capacitance per area was calculated and listed in Table 1; $C_{area\_av} = C_{sp\_av}/A_{BET}$. As seen, large C_{area_av} is estimated in m-WO_{3-x}-C-s electrode (84 μF cm^{-2}), which is smaller than that of m-WO_{3-x}-h (193 μF cm^{-2}) but highly exceed the typical C_{area_av} value in EDLC (≈10 μF cm^{-2}). This indicates that the capacitance of m-WO_{3-x}-C-s is mostly originated from pseudocapacitive charge storage in WO_{3-x} and partial charge accumulation on electric double layer on pure carbon phase occurred together.

In Figure 3b,c, volumetric capacitance (C_{vol}) profiles against voltage were plotted according to an increase of scan rate from 1 to 20 mV s^{-1}. C_{vol} were obtained from dividing specific current by d_{cal} and scan rate. At low scan rates, both electrodes exhibits clear redox peaks and fast current responses at the switching potentials (–0.2 and 0.8 V). As the scan rate increase, however, less distortion of C_{vol} patterns becomes more obvious

Table 1. The physical parameters and electrochemical properties of m-WO_{3-x}-C-s, m-WO_{3-x}-h, CMK-3 and MSP-20 electrodes.

	Surface area [m^2 g^{-1}]	Pore size [nm]	Pore volume [cm^3 g^{-1}]	Pore structure	Origin of capacitance	Capacitance			Electrochemical time constant [e] [s]
						C_{sp_av} [b] [F g^{-1}]	C_{vol_av} [c] [F cm^{-3}]	C_{area_av} [d] [uF cm^{-2}]	
m-WO_{3-x}-C-s[a]	123	12	0.07	Hexagonal (2D)	EDL + Pseudo-capacitance	103	340	84	10.1
m-WO_{3-x}-h	42	3.3, 20	0.18	Cubic (3D)	Pseudo-capacitance	81	254	193	16.1
CMK-3	1300	4	1.01	Hexagonal (2D)	EDL capacitance	132	87	10	6.1
MSP-20	1940	<2	0.89	Random	EDL capacitance	169	122	9	25.5

[a]The m-WO_{3-x}-C-s was synthesized by one step block copolymer self-assembly approach. The m-WO_{3-x}-h and CMK-3 were synthesized by hard template method; [b]Gravimetric capacitance was calculated by using CV data under the 1 mV s^{-1} scan rate; [c]Volumetric capacitance was calculated by using the calculated densities of electrode materials; [d]The capacitance per area is calculated by normalizing the gravimetric capacitance with a BET surface area; [e]Electrochemical time constant was determined by the imaginary capacitance vs. frequency plot.

in m-WO_{3-x}-C-s electrode, which is associated with smaller electrochemical time constant (τ). Theoretically, τ value is proportional to the equivalent series resistance (ESR) and capacitance (C) ($\tau = ESR \times C$).[17,18] When considering higher C, the less distortion of C_{vol} patterns under large scan rate indicates lower ESR value in m-WO_{3-x}-C-s electrode. Probably, this lower ESR is due to improved electrolyte penetration through the ordered mesopores and higher electric conductivity by carbon phase dispersed in nanoscale dimension.

For practical point of view, it is highly desirable that energy density should be attainable even under high power. Especially, volumetric power and energy density have been considered more significant than specific values because there exists strong space limitation on the installations of supercapacitor systems within portable devices and EVs. Thus, the volumetric energy density (E_{vol}) and power density (P_{vol}) were estimated from the CV results (C_{vol}) by using the following equations (Figure 3d):[17]

$$E_{vol}(\nu) = \frac{d_{cal} C_{vol}(\nu) \Delta V^2}{8},$$
$$P_{vol}(\nu) = \frac{E_{vol}(\nu)}{\Delta t(\nu)} = E_{vol}(\nu) \times \frac{\nu}{\Delta V} \quad (2)$$

Here, d_{cal} is the calculated density, ΔV is the voltage range, Δt is the time for the voltage sweep, and ν is the scan rate. The actual power and energy density of the device would be lower because only the active material is considered. Due to the relatively slow Faradaic reaction, it is well known that pseudocapacitors exhibits low power performance when compared with EDLC of high rate capability. In order to compare P_{vol} performances of m-WO_{3-x}-C-s electrode with various EDLC materials, ordered mesoporous carbon (CMK-3,[19] 2D hexagonal mesoporous structure) and conventional activated carbon (MSP-20, random microporous structure) were also employed as supercapacitor electrodes. As shown in Figure 3d, it is observed that abrupt drop of E_{vol} at 1 W cm^{-3} is commonly observed in CMK-3 and MSP-20 electrodes, indicative of fundamental energy limit of electric double layer charging. In addition, obvious E_{vol} decrease is observed in m-WO_{3-x}-h electrode under high power. On the contrary, the E_{vol} of m-WO_{3-x}-C-s becomes well-maintained even under high power condition, reflecting that power performance of m-WO_{3-x}-C-s electrode is significantly improved.[8b]

Figure 4a,b show the galvanostatic charge/discharge profiles of both electrodes measured with different current densities from 1 to 50 mA cm^{-2}. The capacity was obtained by multiplication of the measured current by time. Here, cathodic and anodic directions were defined as downward and upward, respectively. The charge/discharge capacity of the m-WO_{3-x}-C-s electrode is higher than that of the m-WO_{3-x}-h. This tendency corresponds to the results of the CV tests in Figure 3. It is observed that the charge/discharge curve of the m-WO_{3-x}-C-s electrode is close to typical pseudocapacitive triangle shape for both cathodic and anodic direction, which is favorable for uniform charge utilization in the all potential region. On the other hand, the m-WO_{3-x}-h electrode shows a steep voltage increase above 0.3 V, which is related to the abrupt decrease in capacitance in the CV test. With the increase in current density,

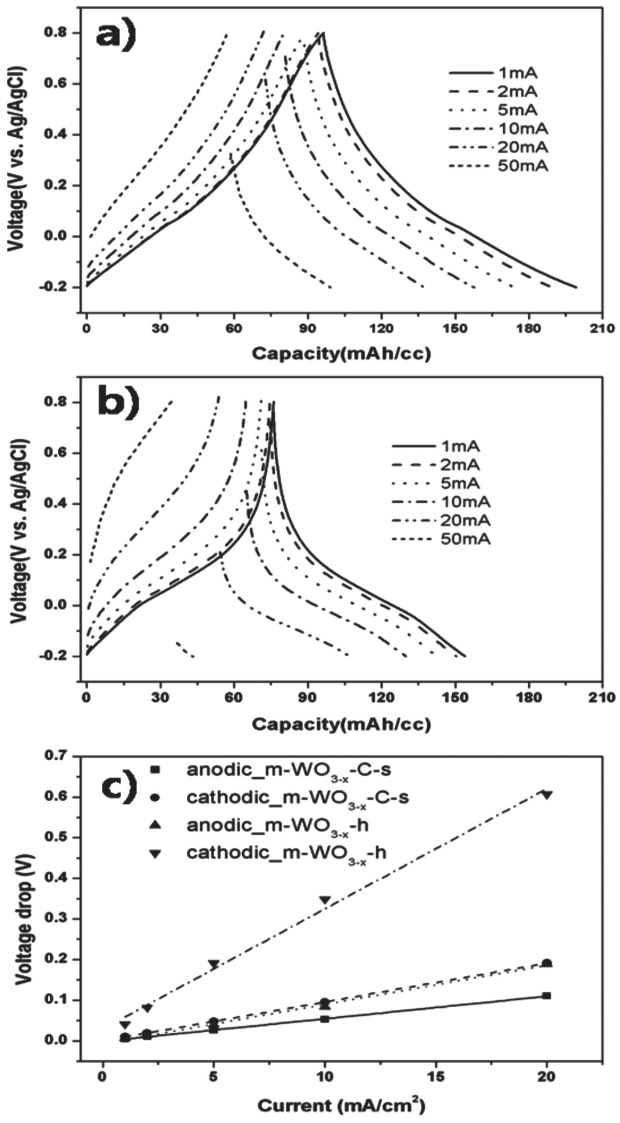

Figure 4. Galvanostatic charge/discharge profiles of a) m-WO_{3-x}-C-s and b) m-WO_{3-x}-h at different current densities (1–50 mA cm^{-2}) in the potential range –0.2 to 0.8 V. c) The IR drops versus the applied current density for m-WO_{3-x}-C-s and m-WO_{3-x}-h electrodes.

furthermore, a capacity decrease is more severe in the m-WO_{3-x}-h electrode. This means that the m-WO_{3-x}-C-s electrode is more advantageous under high current charge/discharge conditions. It has been reported that voltage drop during current switching at –0.2 and 0.8 V is proportional to ESR value.[8e,20] In Figure 4c, change of voltage drop was plotted against current increase. At same current density, clearly, voltage drop of the m-WO_{3-x}-h electrode is bigger (larger ESR) than that of m-WO_{3-x}-C-s. Also note voltage drop of cathodic direction is larger than that of anodic one irrespective of electrode materials, which coincided with our previous results.[9c] For the purpose of direct ESR comparison, ESR was estimated from the slope in Figure 4c. Here, the best fitted lines (solid or dotted) are presented by using the least-squares method. The estimated cathodic and anodic ESR in the m-WO_{3-x}-h electrode are 29.57 and 9.64 Ω,

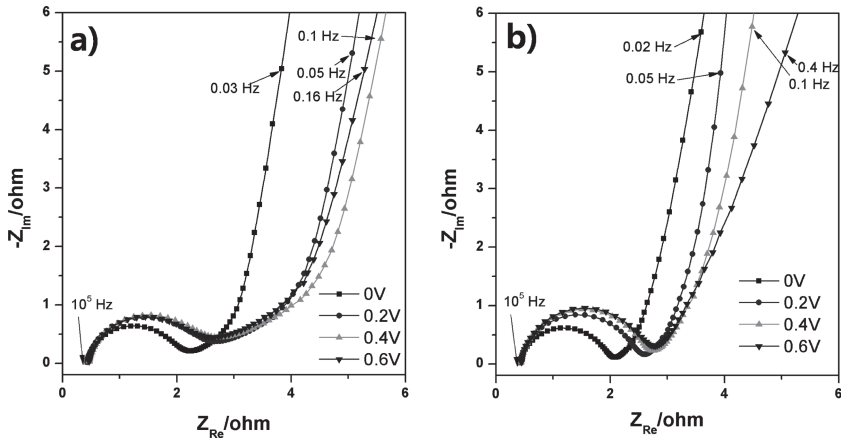

Figure 5. Magnified view of Nyquist plots of a) m-WO_{3-x}-C-s and b) m-WO_{3-x}-h electrodes with voltage changes (0 to 0.6 V). Nyquist plots in 5 mHz to 10^5 Hz range is in Supporting Information Figure S9.

respectively. However, the m-WO_{3-x}-C-s electrode exhibits much lower cathodic (9.54 Ω) and anodic (5.55 Ω) resistances. This ESR difference between employed electrode materials and its dependency on voltage are discussed later.

For the investigation of the electrochemical impedance behavior of our electrodes, electrochemical impedance spectroscopy (EIS) tests were carried out with a change of potential (from 0 to 0.6 V). In **Figure 5**, Nyquist plots in m-WO_{3-x}-h and m-WO_{3-x}-C-s electrodes are shown at various frequency values. As seen, characteristic behaviors for supercapacitors are observed; semi-circle at high frequency, sloped region and steep rise of $-Z_{imag}$ according to decrease of frequency. The semicircle resistance (R_{semi}) at high frequencies can be associated with various resistive phenomena; electrical conduction within electrode, phase-transition resistance from bulk phase into electrode one and resistance associated with pseudocapacitive charge-transfer reaction at WO_{3-x}.[1a] As seen, R_{semi} of m-WO_{3-x}-h electrode gradually increase in accordance with voltage increase. But a slight increase of R_{semi} in m-WO_{3-x}-C-s electrode occurs from 0 to 0.2 V and R_{semi} remains invariant afterward, which is probably relevant to higher electrical conductivity by carbon phase and a complete nanocomposite effect between WO_{3-x} and amorphous carbon. In the sloped region, followed by the semicircle in Figure 5, has been described as the electrolyte penetration through the electrode pores and the proton diffusion into the interphase during pseudocapacitive charging.[21] Interestingly, behavior in the sloped region according to frequency decrease is similar to R_{semi} one, indicating that electrolyte penetration and proton diffusion become less dependent on voltage change especially for m-WO_{3-x}-C-s electrode. This feature becomes more prominent in full frequency region to 0.005 Hz as shown in Figure S9 (Supporting Information). This implies that the complete nanocomposite formation in this material produced higher electrical conductivity, more improved electrolyte transport and better proton diffusion, which resulted in desirable supercapacitor performance.

For further investigation of supercapacitor performance, the impedance data were converted into imaginary capacitance (C_{Im}) plot using following equations:[18,22]

$$C_{Im}(\omega) = \frac{Z_{Re}(\omega)}{\omega \times |Z(\omega)|^2} \quad (3)$$

where $Z_{Re}(\omega)$ is the real part of the complex impedance, respectively, ω is the angular frequency, and $Z(\omega)$ is the complex impedance. From this plot, the characteristic time constants (τ) for quantitative evaluation of the rate capabilities of electrodes can be obtained from the imaginary capacitance and frequency plots (**Figure 6**). From the peak frequency (f_p), the electrochemical time constant can be estimated; $f_p = 0.404/\tau$.[17] As seen in Figure 6, peak shaped patterns are commonly observed and estimated τ values are inserted. As the voltage increase, it is observed that τ became smaller for both electrodes. In Figure 6c, change of τ was plotted against measurement voltage. According to increase of voltage, τ of

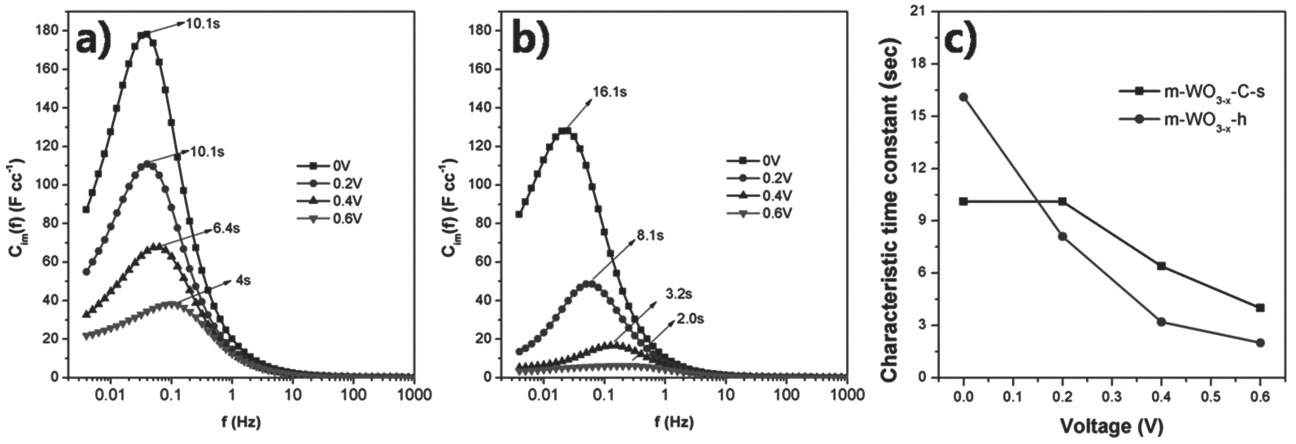

Figure 6. The imaginary part of the complex capacitance (C_{Im}) of a) m-WO_{3-x}-C-s and b) m-WO_{3-x}-h as a function of AC frequency (f) and c) the characteristic time constant versus voltage.

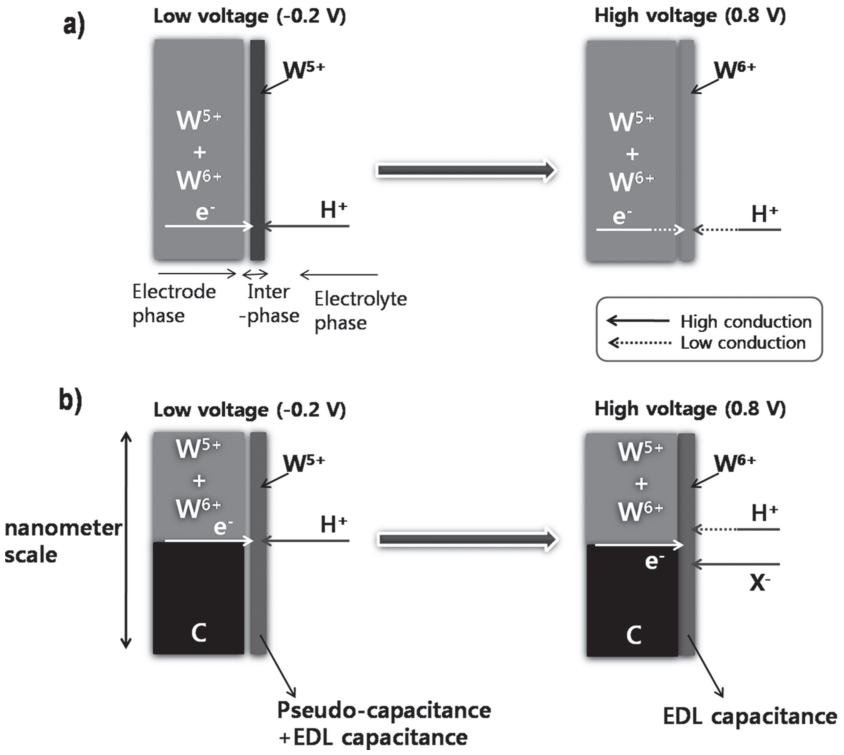

Scheme 2. Graphic explanations of the charge storage mechanism in a) reduced mesoporous tungsten oxide and b) mesoporous tungsten-oxide/carbon composite electrodes.

m-WO_{3-x}-h largely decreases but τ remained less influenced by voltage in m-WO_{3-x}-C-s electrode, which coincides with CV and galvanostatic experiments. When compared with EDLCs such as CMK-3 and MSP-20 electrodes, τ of the m-WO_{3-x}-C-s electrode (10.1 s) is comparable to those of the CMK-3 (6.1 s) and MSP-20 (25.5 s) electrodes tested at 0.2 V (see Figure S10 in the Supporting Information). Hence, it is concluded that m-WO_{3-x}-C-s electrode exhibits a significantly improved charge storage behavior in spite of dominant pseudocapacitive charge storage contribution,[23] which is attributed to high electrical conductivity and well-developed mesoporous structure.

In **Scheme 2**, charge storage mechanism in our m-WO_{3-x}-C-s electrode was elucidated by the comparison with pure pseudocapacitive m-WO_{3-x}-h electrode. In the case of m-WO_{3-x}-h electrode, larger cathodic resistance in high voltage region is relevant to high population of W^{6+} state of tungsten within the interphase, which resulted in low proton diffusivity and large electrical resistance. But abrupt decrease of resistance happens due to transition from W^{6+} to W^{5+} at low voltage. This transition resulted in large change of voltage drop and time constant as shown in Figure 4c and Figure 6c. Also, the W^{5+} population in the bulk phase remains invariant irrespective of applied voltage. Without voltage application, concentration of W^{5+} becomes uniform within whole material. On the contrary to m-WO_{3-x}-h electrode, m-WO_{3-x}-C-s material is a complete nanocomposite between WO_{3-x} and carbon in several nanometer dimensions, as confirmed by our preliminary HR-TEM analysis (Figure S3 in the Supporting Information). Hence, high electrical conductivity by carbon phase can possibly influence on the interphase of m-WO_{3-x} and better electron supply into the interphase is expected. This beneficial effect by carbon phase in nanometer scale can probably alleviate resistance increase resulting from the retarded proton diffusion and low electrical conductivity. Furthermore, the anion charging within electric double-layer in carbon phase is expected to make a capacitive contribution at high potential.

3. Conclusions

In this work, an ordered mesoporous reduced tungsten-oxide/carbon (m-WO_{3-x}-C-s) nanocomposite synthesized by a one-pot soft template approach was employed as an electrode for use in ECs. The m-WO_{3-x}-C-s electrode showed a good volumetric capacitance and fast rate performance, comparable to those of EDLC electrodes. In comparison with partially reduced mesoporous tungsten oxide (m-WO_{3-x}-h), m-WO_{3-x}-C-s exhibited improved capacitance and decreased internal resistance because of the advantageous properties of amorphous carbon, i.e., enhanced electrical and proton conduction. This study implies that a well-mixed and nanosized metal-oxide/carbon composite approach is one way of improving the rate performance of transition metal oxide electrode materials. In addition, the 12 nm sized large pores (derived from large molecular weight PS-*b*-PEO) also contributed to the improved rate performance. This facile soft template approach, employing lab-synthesized block copolymers, can be extended to other transition metal oxide/carbon composite materials for the synthesis of high-performance electrode materials for ECs.

4. Experimental Section

Materials: The poly(styrene-*b*-ethylene oxide) block copolymer (PS-*b*-PEO) was synthesized via atom-transfer radical polymerization (ATRP) following the reported procedure.[12] The Mn value of PS-*b*-PEO was 15,600 g mol^{-1} (32 wt% PEO) and its polydispersity index was 1.26. The resol precursor was prepared by a basic polymerization method.[24] Tungsten chloride (WCl_6, 99.9%), anhydrous chloroform, and anhydrous ethanol were purchased from Aldrich and used without further purification.

Synthesis of m-WO_{3-x}-C-s: In a typical synthesis, 0.15 g of PS-*b*-PEO was dissolved in 10 mL of anhydrous chloroform. Tungsten chloride (WCl_6, 0.13 g) was mixed with the polymer solution. Subsequently, 0.1 g of resol precursor (20 wt% in THF) was added to the polymer/metal precursor solution. After vigorous stirring for 10 min, 0.2 mL of anhydrous ethanol was added slowly to the solution, and the mixture was stirred vigorously for 4 h. The resultant mixture was transferred to a Petri dish on a hot plate at 50 °C for 8 h, and dried at 100 °C in an oven for 8 h. The as-prepared films were calcined at 700 °C for 2 h (1 °C min^{-1}).

Characterization: Powder XRD patterns were identified using a Bruker D8 Advance X-ray diffractometer (Cu Kα radiation). XPS data were obtained with a VG Scientific Escalab 250 using an Al Kα X-ray source. SAXS patterns were measured using 4C SAXS beamline at the

Pohang Light Source (PLS). The structures were examined using TEM with a JEM-1011 microscope (Jeol LTD) and SEM with an S-4200 field-emission SEM (Hitachi). The surface area and pore size distribution were calculated from the nitrogen sorption isotherms at 77 K using a Tristar II 3020 instrument (Micromeritics Instrument Corporation).

Electrochemical Characterization: For the preparation of working electrodes, the active materials, tungsten-oxide/carbon composite, and partially reduced mesoporous tungsten oxide (for control experiment) were mixed with the carbon additive Ketjenblack ECP-600JD (KB) and polytetrafluoroethylene (PTFE) binder (10:1:1 in weight ratio) in isopropyl alcohol. The mixtures were coated on a stainless steel Exmet current collector (1 cm × 1 cm). The resulting electrode plates were pressed and dried under vacuum at 100 °C for 12 h.

The electrochemical performance of the m-WO_{3-x}-C-s electrode was analyzed using a cell with a three-electrode configuration in aqueous 2 M H_2SO_4 electrolyte. A Pt wire and Ag/AgCl electrode were used as the counter and reference electrodes, respectively. The inter-electrode gap between the reference and working electrodes was fixed as 0.5 cm. Cyclic voltammetry (CV) and electrochemical impedance spectroscopy (EIS) were carried out using a Reference 600 potentiostat (Gamry Instruments, USA). CV tests were performed in the potential range –0.2 to 0.8 V (vs. Ag/AgCl). The EIS data were recorded at 10-mV magnitude at frequencies from 0.005 to 10^5 Hz (0 to 0.6 V). Galvanostatic charge/discharge profiles in the potential range –0.2 to 0.8 V (vs. Ag/AgCl) were measured for current densities of 1 to 50 mA cm^{-2} using a WBCS-3000 battery cycler (Xeno Co.).

Supporting Information

Supporting Information is available from the Wiley Online Library or from the author.

Acknowledgements

This work was supported by the National Research Foundation of Korea (NRF) grant funded by the Korea government (MEST) (No. 2012R1A2A2A01002879) and the Korea Institute of Science and Technology (KIST) Institutional Program (2E22853-12-105). This work was further supported by the Global Frontier R&D Program on Center for Multiscale Energy System funded by the National Research Foundation under the Ministry of Education, Science and Technology, Korea.

Received: September 16, 2012
Revised: December 21, 2012
Published online: March 13, 2013

[1] a) B. E. Conway, *Electrochemical supercapacitors: scientific fundamentals and technological applications*, Kluwer Academic/Plenum, New York **1999**; b) J. R. Miller, P. Simon, *Science* **2008**, *321*, 651; c) P. Simon, Y. Gogotsi, *Nat. Mater.* **2008**, *7*, 845.

[2] a) S. H. Oh, L. F. Nazar, *J. Mater. Chem.* **2010**, *20*, 3834; b) C.-C. Hu, K.-H. Chang, M.-C. Lin, Y.-T. Wu, *Nano Lett.* **2006**, *6*, 2690; c) W. Sugimoto, H. Iwata, K. Yokoshima, Y. Murakami, Y. Takasu, *J. Phys. Chem. B* **2005**, *109*, 7330; d) Q. Lu, M. W. Lattanzi, Y. Chen, X. Kou, W. Li, X. Fan, K. M. Unruh, J. G. Chen, J. Q. Xiao, *Angew. Chem. Int. Ed.* **2011**, *123*, 6979; e) T. Xue, C.-L. Xu, D.-D. Zhao, X.-H. Li, H.-L. Li, *J. Power Sources* **2007**, *164*, 953; f) B. Wang, J. S. Chen, Z. Wang, S. Madhavi, X. W. Lou, *Adv. Energy Mater.* **2012**, *2*, 1188.

[3] a) Y. G. Wang, H. Q. Li, Y. Y. Xia, *Adv. Mater.* **2006**, *18*, 2619; b) J.-H. Kim, Y.-S. Lee, A. K. Sharma, C. G. Liu, *Electrochim. Acta* **2006**, *52*, 1727.

[4] a) J. Yan, E. Khoo, A. Sumboja, P. S. Lee, *ACS Nano* **2010**, *4*, 4247; b) S. Chen, J. Zhu, X. Wu, Q. Han, X. Wang, *ACS Nano* **2010**, *4*, 2822; c) Y.-T. Kim, K. Tadai, T. Mitani, *J. Mater. Chem.* **2005**, *15*, 4914; d) G. Yu, L. Hu, M. Vosgueritchian, H. Wang, X. Xie, J. R. McDonough, X. Cui, Y. Cui, Z. Bao, *Nano Lett.* **2011**, *11*, 2905; e) X. Lang, A. Hirata, T. Fujita, M. Chen, *Nat. Nanotechnol.* **2011**, *6*, 232; f) J. H. Jang, S. Han, T. Hyeon, S. M. Oh, *J. Power Sources* **2003**, *123*, 79.

[5] a) Y. B. He, G. R. Li, Z. L. Wang, C. Y. Su, Y. X. Tong, *Energy Environ. Sci.* **2011**, *4*, 1288; b) S. A. Sherrill, J. Duay, Z. Gui, P. Banerjee, G. W. Rubloff, S. B. Lee, *Phys. Chem. Chem. Phys.* **2011**, *13*, 15221; c) D. Liu, Q. Wang, L. Qiao, F. Li, D. Wang, Z. Yang, D. He, *J. Mater. Chem.* **2012**, *22*, 483.

[6] a) G. Leftheriotis, S. Papaefthimiou, P. Yianoulis, A. Siokou, *Thin Solid Films* **2001**, *384*, 298; b) B. X. Zou, Y. Liang, X. X. Liu, D. Diamond, K. T. Lau, *J. Power Sources* **2011**, *196*, 4842; c) D. Wang, J. Li, X. Cao, G. Pang, S. Feng, *Chem. Commun.* **2010**, *46*, 7718; d) C. C. Huang, W. Xing, S. P. Zhuo, *Scripta Mater.* **2009**, *61*, 985; e) X. Lu, T. Zhai, X. Zhang, Y. Shen, L. Yuan, B. Hu, L. Gong, J. Chen, Y. Gao, J. Zhou, Y. Tong, Z. L. Wang, *Adv. Mater.* **2012**, *24*, 938.

[7] H. Wang, X. Dong, S. Peng, L. Dong, Y. Wang, *J. Alloys Compd.* **2012**, *527*, 204.

[8] a) J. Lee, S. Yoon, T. Hyeon, S. M. Oh, K. B. Kim, *Chem. Commun.* **1999**, 2177; b) S. Yoon, J. Lee, T. Hyeon, S. M. Oh, *J. Electrochem. Soc.* **2000**, *147*, 2507; c) W. Li, D. Chen, Z. Li, Y. Shi, Y. Wan, G. Wang, Z. Jiang, D. Zhao, *Carbon* **2007**, *45*, 1757; d) S. Xiong, C. Yuan, X. Zhang, B. Xi, Y. Qian, *Chem. Eur. J.* **2009**, *15*, 5320; e) C. Jo, S. An, Y. Kim, J. Shim, S. Yoon, J. Lee, *Phys. Chem. Chem. Phys.* **2012**, *14*, 5695; f) T. Brezesinski, J. Wang, S. H. Tolbert, B. Dunn, *Nat. Mater.* **2010**, *9*, 146.

[9] a) E. Kang, S. An, S. Yoon, J. K. Kim, J. Lee, *J. Mater. Chem.* **2010**, *20*, 7416; b) S. Yoon, E. Kang, J. K. Kim, C. W. Lee, J. Lee, *Chem. Commun.* **2011**, *47*, 1021; c) C. Jo, I. Hwang, J. Lee, C. W. Lee, S. Yoon, *J. Phys. Chem. C* **2011**, *115*, 11880; d) S. Yoon, C. Jo, S. Y. Noh, C. W. Lee, J. H. Song, J. Lee, *Phys. Chem. Chem. Phys.* **2011**, *13*, 11060.

[10] J. Lee, J. Kim, T. Hyeon, *Adv. Mater.* **2006**, *18*, 2073.

[11] J. Lee, Y. S. Jung, S. C. Warren, M. Kamperman, S. M. Oh, F. J. DiSalvo, U. Wiesner, *Macromol. Chem. Phys.* **2011**, *212*, 383.

[12] J. Hwang, J. Kim, E. Ramasamy, W. Choi, J. Lee, *Microporous Mesoporous Mater.* **2011**, *143*, 149.

[13] a) T. Yu, Y. H. Deng, L. Wang, R. L. Liu, L. J. Zhang, B. Tu, D. Y. Zhao, *Adv. Mater.* **2007**, *19*, 2301; b) L. X. Song, M. Wang, S. Z. Pan, J. Yang, J. Chen, J. Yang, *J. Mater. Chem.* **2011**, *21*, 7982; c) W. Cui, F. Wang, J. Wang, H. Liu, C. Wang, Y. Xia, *J. Power Sources* **2011**, *196*, 3633.

[14] S. Shi, X. Xue, P. Feng, Y. Liu, H. Zhao, T. Wang, *J. Cryst. Growth* **2008**, *310*, 462.

[15] P. T. Tanev, T. J. Pinnavaia, *Science* **1995**, *267*, 865.

[16] F. Su, J. Zeng, X. Bao, Y. Yu, J. Y. Lee, X. S. Zhao, *Chem. Mater.* **2005**, *17*, 3960.

[17] J. H. Jang, A. Kato, K. Machida, K. Naoi, *J. Electrochem. Soc.* **2006**, *153*, A321.

[18] P. L. Taberna, P. Simon, J. F. Fauvarque, *J. Electrochem. Soc.* **2003**, *150*, A292.

[19] S. Jun, S. H. Joo, R. Ryoo, M. Kruk, M. Jaroniec, Z. Liu, T. Ohsuna, O. Terasaki, *J. Am. Chem. Soc.* **2000**, *122*, 10712.

[20] K. H. An, K. K. Jeon, J. K. Heo, S. C. Lim, D. J. Bae, Y. H. Lee, *J. Electrochem. Soc.* **2002**, *149*, A1058.

[21] J. Gamby, P. L. Taberna, P. Simon, J. F. Fauvarque, M. Chesneau, *J. Power Sources* **2001**, *101*, 109.

[22] C. Portet, G. Yushin, Y. Gogotsi, *Carbon* **2007**, *45*, 2511.

[23] a) J.-H. Sung, S.-J. Kim, K.-H. Lee, *J. Power Sources* **2004**, *133*, 312; b) D. Wei, M. R. J. Scherer, C. Bower, P. Andrew, T. Ryhänen, U. Steiner, *Nano Lett.* **2012**, *12*, 1857.

[24] Y. Meng, D. Gu, F. Zhang, Y. Shi, H. Yang, Z. Li, C. Yu, B. Tu, D. Zhao, *Angew. Chem. Int. Ed.* **2005**, *117*, 7215.